SIAM J. Applied Dynamical Systems
Vol. 19, No. 3, pp. 2135–2161

Entrainment Dynamics of Forced Hierarchical Circadian Systems Revealed by 2-Dimensional Maps*

Guangyuan Liao†, Casey Diekman†, and Amitabha Bose†

Abstract. The ability of a circadian system to entrain to the 24-hour light-dark cycle is one of its most important properties. A new tool, called the entrainment map, was recently introduced to study this process for a single oscillator. Here we generalize the map to study the effects of light-dark forcing in a hierarchical system consisting of a central circadian oscillator that drives a peripheral circadian oscillator. We develop techniques to reduce the higher-dimensional phase space of the coupled system to derive a generalized two-dimensional entrainment map. Determining the nature of various fixed points, together with an understanding of their stable and unstable manifolds, leads to conditions for existence and stability of periodic orbits of the circadian system. We use the map to investigate how various properties of solutions depend on parameters and initial conditions including the time to and direction of entrainment. We show that the concepts of phase advance and phase delay need to be carefully assessed when considering hierarchical systems.

Key words. circadian rhythm, limit cycle, Poincaré map, coupled oscillators

AMS subject classifications. 37E10, 92B25

DOI. 10.1137/19M1307676

1. Introduction.

Circadian rhythms refer to a variety of oscillatory processes that occur over a roughly 24-hour time period. Circadian oscillations are found in a variety of animal and plant species [5]. Within humans a common example involves our core body temperature which shows a local minimum typically in the early morning hours ($\sim$ 4:00 AM) and a local maximum roughly twelve hours later [25]. Similarly, concentrations of certain hormone levels within our bodies oscillate over the course of a day [12]. In the absence of any explicit forcing from naturally occurring light-dark cycles, circadian oscillators possess endogenous periods of roughly 24 hours. Their ability to also entrain to 24-hour periodic cycles of light and dark is one of their most important properties.

The entrainment of circadian oscillators has been mathematically analyzed using a variety of techniques. Often this involves describing the circadian oscillator with a reduced phase description such as that given by a Kuramoto oscillator [7, 27]. The problem then reduces to studying periodically forced Kuramoto systems. Other approaches include deriving model equations that retain more of their connection to the underlying biological process [36, 41]. Recently Diekman and Bose [13] introduced a novel tool called the entrainment map to de-

*Received by the editors December 18, 2019; accepted for publication (in revised form) by J. Rubin July 2, 2020; published electronically September 15, 2020.
https://doi.org/10.1137/19M1307676
Funding: The work of the second author was partially supported by NSF grant DMS-1555237 and U.S. Army Research Office grant W911NF-16-1-0584.
†Department of Mathematical Sciences, New Jersey Institute of Technology, Newark, NJ 07102 (gl92@njit.edu, casey.o.diekman@njit.edu, bose@njit.edu).

termine whether a circadian oscillator can entrain to the 24-hour light-dark cycle and, if so, at what phase. The derived map is equivalent to a 1-dimensional (1-D) Poincaré map that tracks the phase of light onset of the light-dark forcing on a cycle-by-cycle basis. In principle, the dimension of the underlying circadian oscillator model is not relevant. Diekman and Bose derived entrainment maps for the 2-dimensional (2-D) Novák–Tyson model [41, 36], the 3-dimensional (3-D) Gonze model [18], and the 180-D Kim–Forger model [22]. In general, the map can be used to estimate both entrainment times and whether entrainment occurs through phase advance or delay with respect to the daily onset of lights.

There are several scenarios in which circadian oscillators do not directly receive light-dark forcing [18, 20, 29]. Instead they are part of hierarchical systems in which, as "peripheral" oscillators, they are periodically forced by other "central" circadian oscillators that do directly receive light input. Cells within major organs in our bodies fall into this category. Several natural questions arise about the entrainment process of these peripheral oscillators. For example, do they entrain through phase advance or phase delay as central oscillators do? To what extent is their entrainment time dependent on the entrainment process of the central oscillator from which they receive forcing? To study such questions, here we generalize the entrainment map to a 2-D map where we track from the perspective of the peripheral oscillator both the phase of the central oscillator as well as the phase of light onset.

In this paper, we first consider the situation in which a single central oscillator receives light-dark input. In turn, this central oscillator sends input to a single peripheral oscillator. To focus on the mathematical aspects of the derivation and analysis of the 2-D entrainment map, we will utilize the planar Novák–Tyson model [36] for both the central and peripheral oscillators. The phase space for this problem is 5-dimensional (5-D), two for each of the oscillators and a fifth that accounts for the light-dark forcing. We will define a Poincaré section transversal to the flow allowing us to derive a 2-D map that determines the phase of light and the phase of the central oscillator at each cycle when the peripheral oscillator lies on the Poincaré section. We analyze the map by extending techniques first introduced in Akcay, Bose, and Nadim [1] and Akcay et al. [2]. We will show that for a range of parameter values, the map possesses four fixed points: one asymptotically stable and three unstable fixed points, two of which are saddle points. All of these fixed points are related to actual periodic orbits of the flow. By numerically calculating entrainment times (defined precisely later in the text), we are able to uncover how the stable and unstable manifolds of the saddle points organize the iterates of the map, determine the direction of entrainment, and give rise to a rich set of dynamics. The findings of the map are then validated by comparing them to direct simulations of the model equations. We also extend the analysis to the case of a semihierarchical system that consists of a second central oscillator that receives less light input than the first central oscillator.

Analysis of the map reveals several important insights into the entrainment and reentrainment process. First, bounds on important parameters, such as the intensity of light input and the strength of the coupling from the central oscillator that lead to entrainment, are easily identified. We are able to determine which kinds of perturbations lead to faster or slower reentrainment, e.g., whether perturbations that desynchronize only the peripheral oscillator but not the central one lead to quick reconvergence. Interestingly, we find that the straightforward notion of convergence via phase advance or phase delay needs to be generalized. Indeed, the peripheral oscillator can converge by a combination of phase advance and delay while the central

oscillator typically converges by either phase advancing or delaying. This result has implications for recovery from jet lag and abrupt changes in sleep-wake schedules. In experimental studies of aircrews, some subjects experienced internal dissociation with different components of the circadian system converging in opposite directions [23]. Specifically, after an eastbound flight across 9 time zones, activity rhythms reentrained through phase advances while body temperature reentrained through phase delays. In hospital studies, a 12-hour phase shift of sleep time results in a phase advance of urinary potassium but a phase delay in urinary hydroxycorticosteroids [31]. Aschoff [4] referred to this behavior as "reentrainment by partition" and suggested that it may impact health and contribute to the degradation of psychomotor performance observed on postflight days. The saddle fixed points of our map provide a dynamical explanation for the partitioning phenomenon, as will be elaborated upon in the discussion.

2. Models and methods.

Our model is based on the Novák–Tyson (NT) model [41] for the molecular circadian clock in the fruit fly *Drosophila*. The NT model can be written in the following form:

$$\begin{aligned} \frac{1}{\phi}\frac{dP}{dt} &= M - k_f h(P) - k_D P - k_L f(t) P, \\ \frac{1}{\phi}\frac{dM}{dt} &= \epsilon\left(g(P) - M\right), \end{aligned} \tag{1}$$

where $g(P) = \frac{1}{1+P^4}$, and $h(P) = \frac{P}{0.1+P+2P^2}$. The M variable represents mRNA concentration, and P variable represents the protein concentration. The parameter ϵ is small, which separates P and M into fast and slow variables. The parameter ϕ will directly affect the period of the solutions of this system; smaller values imply longer endogenous periods. The function $f(t)$ describes the light-dark (LD) forcing, which is defined by a 24-hour periodic step function, $f(t) = 1$ when lights are on and $f(t) = 0$ when lights are off. We consider for convenience a 12:12 photoperiod. There is no difficulty in extending to other photoperiods, though a minimum amount of light per day is needed for entrainment; see [13] for a detailed assessment of how entrainment depends on photoperiod and light intensity. In *Drosophila*, there is protein degradation during darkness, and light increases the degradation. So k_D represents the degradation rate during darkness, and k_L represents the additional degradation rate which is caused by light. The parameter k_f is a combination of two variables in the original Tyson et al. paper [41]. In [13], the entrainment of a single NT oscillator to a 24-hour period LD forcing was studied. The ensuing solution was denoted as an LD-entrained solution.

2.1. Coupled NT model.

The coupled NT (CNT) model is given by the following equations:

$$\begin{aligned} \frac{1}{\phi_1}\frac{dP_1}{dt} &= M_1 - k_f h(P_1) - k_D P_1 - k_{L_1} f(t) P_1, \\ \frac{1}{\phi_1}\frac{dM_1}{dt} &= \epsilon[g(P_1) - M_1], \\ \frac{1}{\phi_2}\frac{dP_2}{dt} &= M_2 - k_f h(P_2) - k_D P_2 - k_{L_2} f(t) P_2, \\ \frac{1}{\phi_2}\frac{dM_2}{dt} &= \epsilon[g(P_2) - M_2 + \alpha_1 M_1 g(P_2)]. \end{aligned} \tag{2}$$

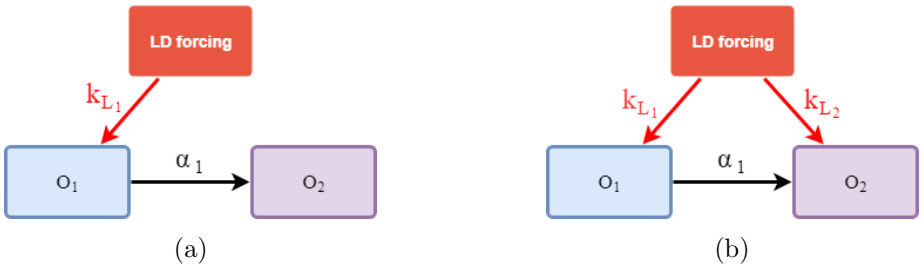

Figure 1. (a) *Model with strict hierarchical coupling.* (b) *Semihierarchical model when both oscillators receive light input, but the light into O_2 is much weaker than the light into O_1.*

The parameters and variables have the same meaning as the original NT model. We introduce a coupling term $\alpha_1 M_1 g(P_2)$, from oscillator 1 (O_1) to oscillator 2 (O_2). The parameter α_1 is a nonnegative real number which denotes the coupling strength. We placed the coupling factor into the second equation of O_2 based on Roberts et al. [39], who suggest that coupling occurs between the mRNA production rates.

We mainly study the case with strict hierarchical coupling, which is shown in Figure 1(a). In this case, the LD forcing is applied only on O_1, which then has feedforward coupling onto O_2. We fix the value of parameter $k_{L_2} = 0$. Figure 1(b) shows the semihierarchical CNT model when both oscillators receive light forcing, but the effect of light into O_2 is taken to be less intense than that into O_1; in other words, $k_{L_2} < k_{L_1}$.

2.2. The entrainment map. When attempting to determine the existence of periodic solutions using Poincaré maps, one has to decide where in phase space to place the section. Often in circadian models, the Poincaré section is placed on the 24-hour LD forcing, leading to a stroboscopic map that determines the state of the system every 24 hours. In [13], Diekman and Bose instead placed the section in the phase space of the circadian oscillator and backed out the phase of light when the oscillator was at the section. Here, we follow that approach when building the 2-D map. The Poincaré section is chosen at a location in the flow that O_2 will be shown to cross. In this section, we first introduce the original 1-D map, and then generalize it to our 2-D map.

The entrainment map $\Pi(y)$ for the original NT model was introduced as a 1-D map in [13]. To define $\Pi(y)$, Diekman and Bose take a Poincaré section $\mathcal{P}$ as a 1-D line segment which intersects the LD-entrained solution of a single periodically forced NT oscillator. The section is placed along a portion of an attracting 1-D slow manifold where all trajectories of the NT oscillator pass. A phase variable y is defined to be the amount of time that has passed since the beginning of the most recent LD cycle. When the trajectory first returns to $\mathcal{P}$, the map $\Pi(y)$ is defined to be the amount of time that has passed since the onset of the most recent LD cycle, which is the new phase of the light forcing. The domain and range of $\Pi(y)$ are both (0,24]. The domain is actually homeomorphic to the unit circle $\mathbb{S}^1$, so $y = 0$ and $y = 24$ are equivalent. The map is written as $y_{n+1} = \Pi(y_n)$, where

$$\Pi(y_n) = (\rho(y_n) + y_n) \bmod 24. \tag{3}$$

$\rho(y)$ is a return time map that measures the time a trajectory starting on $\mathcal{P}$ takes to return

to $\mathcal{P}$. It is continuous and periodic at its endpoints $\rho(0^+) = \rho(24^-)$. If $\rho(y) < 24 - y$, then $\Pi(x) = \rho(y) + y$, because the trajectory will return back to $\mathcal{P}$ within the same LD cycle which it started. If $24 - y < \rho(y) < 48 - y$, then $\Pi(y) = \rho(y) + y - 24$, because the trajectory will return in the next LD cycle and so on.

If there exists a y_s such that $y_s = \Pi(y_s)$ and $|\Pi'(y_s)| < 1$, then y_s is a stable fixed point of the map $\Pi(y)$, and it also determines a 1:1 phase locked solution. The phenomenon of 1:1 phase locking in this case occurs when the oscillator has one return to the Poincaré section for every one period of the LD forcing. When a stable solution exists, the map $\Pi(y)$ quite accurately calculates the time to approach the stable solution starting from any initial condition of y. Numerically we use the concept of entrainment to evaluate the convergence time. Suppose y_j is a sequence of iterates of the map, then we say the solution is entrained if there exists m, such that for all $j \geq m$, $|y_s - y_j| < 0.5$. The entrainment time is then $\Sigma_{i=1}^{m} \rho(y_i)$.

The 1-D O_1-entrained map for the CNT system. The 1-D map for the NT system cannot be directly applied to the CNT system because the second oscillator will have additional free variables to determine, meaning that the entrainment map for the CNT system will be higher dimensional. However, for the hierarchical CNT system, if we assume that O_1 is already entrained, then the chain $LD \Rightarrow O_1 \Rightarrow O_2$ is reduced to O_1-entrained $\Rightarrow O_2$. The system can be rewritten in the following manner:

$$\begin{aligned} \frac{1}{\phi_2}\frac{dP_2}{dt} &= M_2 - k_f h(P_2) - k_D P_2, \\ \frac{1}{\phi_2}\frac{dM_2}{dt} &= \epsilon[g(P_2) - M_2 + \alpha_1 M_1 g(P_2)]. \end{aligned} \tag{4}$$

In the O_1-entrained case, O_2 is continuously forced by the coupling from O_1. This differs from the coupling due to direct light input into O_1 which is a discontinuous square wave. We place a Poincaré section that intersects the entrained O_2 limit cycle solution at $\mathcal{P} : P_2 = 1.72, |M_2 - 0.1289| < \delta$ such that $P_2' < 0$, where δ is a small control parameter. In the results section, we will explain why trajectories are funneled into a region that forces them to cross this choice of Poincaré section. Along the section $\mathcal{P}$, P_2 is fixed, and M_2 is bounded by δ, so the only free variable is the phase of light. We define the 1-D O_1-entrained map by

$$y_{n+1} = \Pi_{O_1}(y_n) = (y_n + \rho(y_n; \gamma(y_n))) \bmod 24, \tag{5}$$

where $y \in (0, 24]$ is defined to be the phase of the LD forcing, which has the same meaning as the 1-D entrainment map in [13]. We define $\gamma(t) := \varphi_t(X_0)$ to be the LD-entrained limit cycle of O_1, where X_0 is a chosen reference point on $\gamma(t)$. We denote the set of points that lie on the limit cycle of O_1 by Γ_{O_1}. At X_0, the lights just turn on for O_1. In the O_1-entrained case, the location of O_1 only depends on y_n and can be denoted by $\gamma(y_n)$. Based on the above definition, $\gamma(y_n)$ means a point on the limit cycle of O_1 when the light has been turned on for y_n hours. $\rho(y_n)$ measures the return time when O_2 first returns $\mathcal{P}$.

Notice that in the definition of the O_1-entrained map, the phase of O_1 is determined by y (the phase of the LD forcing), since it is O_1-entrained. This makes the O_1-entrained map a 1-D map, and most of the properties of the NT model's 1-D map carry over to the O_1-entrained

map. For example, if there is a point y_s, such that $y_s = \Pi_{O_1}(y_s)$ and $|\Pi'_{O_1}(y_s)| < 1$, then y_s is a stable fixed point of the O_1-entrained map. The fixed points of the map also determine 1:1 phase locked solutions of the coupled system.

The general 2-D entrainment map. In the case of the O_1-entrained map, the initial location of O_1 when O_2 lies on $\mathcal{P}$ is always determined by y, the phase of the LD cycle. But in general, the initial location of O_1 doesn't always depend on y, rather it could lie arbitrarily in its phase space. To limit the possibilities, we restrict the initial location of O_1 to lie anywhere along its own limit cycle Γ_{O_1}. This restriction will therefore only introduce one new free variable and motivates us to generalize the map to two dimensions:

$$(x_{n+1}, y_{n+1}) = \Pi(x_n, y_n) = (\Pi_1(x_n, y_n), \Pi_2(x_n, y_n)).$$

We keep the definition of y_n and the location of the Poincaré section $\mathcal{P}$ the same as in the O_1-entrained map. We now introduce a new variable x to determine O_1's position in phase space relative to its own LD-entrained solution. The detailed definition is explained using a phase angle.

Defining Π_1 using a phase angle. According to the O_1-entrained map, the trajectory of O_1 always remains on Γ_{O_1}. However, if O_1 is not already entrained, then its trajectory may not lie on Γ_{O_1} but will instead approach it asymptotically. Thus we need a new independent variable to determine the position of O_1 for this situation. From the O_1-entrained case, the position of O_1 can always be described as $\gamma(t)$, where $t \in (0, 24]$. The idea is to define a new independent phase variable x equivalent to the time variable t that is obtained by projecting the real location of O_1 onto its limit cycle Γ_{O_1}, while keeping the error small. We define the phase angle in the following steps:

(1) Transform the coordinate system appropriately: Shift the origin to the intersection point of the uncoupled O_1's two nullclines. Then connect the origin and the point X_0 and expand the line segment as the x-axis of the new coordinate system. The y-axis is determined automatically to be orthogonal to the x-axis, as in Figure 2(a).

(2) Define x in terms of the phase angle: Consider the phase plane as a complex plane $\mathbb{C}$. Let's call the point X_0 as $z_0 = r_0 e^{i\theta_0} \in \mathbb{C}$, where $\theta_0 = 0$ after the coordinate system transformation. We can then represent any point on the limit cycle $\gamma(t)$ as a complex number $z = re^{i\theta}$, where we define $\theta \in (0, 2\pi]$. Then x is defined to be the phase of O_1 when choosing X_0 as the reference point. In other words, $z = \gamma(x) = re^{i\theta}$. Notice that x is homeomorphic to the unit circle $\mathbb{S}^1$, because $\theta = Arg(\gamma(x))$; see Figure 2(a). The domain of x is also $\tilde{\mathbb{S}}^1 = (0, 24]$.

(3) Define the map Π_1. Suppose we start integrating the system with any initial condition (x_n, y_n) (see Figure 2(a), lower panel as an example). After the time $\rho(x_n, y_n)$, O_2 returns to the Poincaré section, the new location of O_1 is now

$$\Psi_{\rho(x_n,y_n)}(\gamma(x_n)) = r_{n+1} e^{i\theta_{n+1}},$$

where $\Psi_t(X)$ is the flow of O_1, and the phase angle is θ_{n+1}. We then find the unique point $\hat{x}$ lying on Γ_{O_1} such that the phase angle of $\Psi_{\rho(x_n,y_n)}(\gamma(x_n))$ matches the angle associated with $\gamma(\hat{x})$. That is we choose $\hat{x}$ such that $Arg(\gamma(\hat{x})) = \theta_{n+1}$. Geometrically, we are simply choosing $\hat{x}$ as the associated value at which the ray passing through $\Psi_{\rho(x_n,y_n)}(\gamma(x_n))$ intersects $\gamma(t)$.

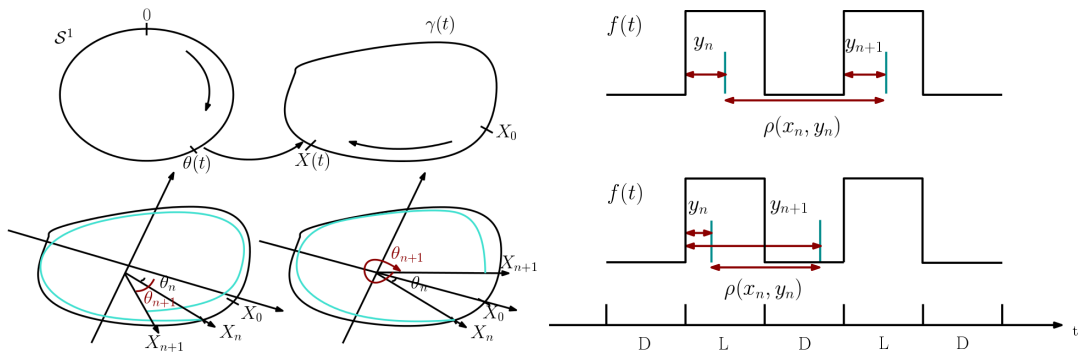

(a) Schematic for Π_1 (b) Schematic for Π_2

Figure 2. (a) *The upper panel shows a schematic of the homeomorphism from the unit circle* $\mathbb{S}^1$ *to* Γ_{O_1}. *The lower panel shows how we construct the map in two different conditions; the left one shows the case when the phase angle* θ *associated with the trajectory of* O_1 *rotates through more than* 2π, *the right one is where the rotation is less than* 2π. (b) *In both panel schematics, the first blue vertical line segment denotes where we chose the initial phase of light. After time* $\rho(x_n, y_n)$, *the trajectory returns to* $\mathcal{P}$, *and the new phase of light is* y_{n+1}. *For the upper panel,* $y_n + \rho(x_n, y_n) > 24$, *so* $y_{n+1} = y_n + \rho(x_n, y_n) - 24$. *For the lower panel,* $y_n + \rho(x_n, y_n) < 24$, *so* $y_{n+1} = y_n + \rho(x_n, y_n)$. *The black square wave* $f(t)$ *in both panels represents the LD forcing.*

We define $x_{n+1} = \hat{x}$. We can then write Π_1 as the following:

$$x_{n+1} = \Pi_1(x_n, y_n) = \{\hat{x} \in [0, 24) : Arg(\gamma(\hat{x})) = \theta_{n+1}\}. \tag{6}$$

(4) To numerically compute the map Π_1, we integrate an initial condition where O_1 lies along its limit cycle and O_2 at $\mathcal{P}$, and integrate the system until O_2 returns to the section. We then use a linear map to shift the new location of O_1 to the coordinate system we set up in step 1. We transform the point into a complex number, and then use the built-in MATLAB function *angle()* to find the phase angle. Using this angle, we locate a point on the limit cycle of O_1, that we had previously partitioned, with the same phase angle.

The definition of Π_2 is straightforward. We just mimic the construction of the O_1-entrained map. The only difference is that the return time function ρ depends on both x and y, because O_1 is no longer O_1-entrained:

$$y_{n+1} = \Pi_2(x_n, y_n) = y_n + \rho(x_n, y_n) \bmod 24, \tag{7}$$

where $y \in \tilde{\mathbb{S}}^1 = (0, 24]$ is defined on a homeomorphism of the unit circle $\mathbb{S}^1$, $y = h(\theta) = \frac{12}{\pi} \times \theta$.

The schematic Figure 2(b) depicts a way to understand the definition of Π_2. The first blue vertical line segment signifies the initial phase y_n of the lights when O_2 starts on $\mathcal{P}$. After time $\rho(x_n, y_n)$, the trajectory returns to $\mathcal{P}$, signified by the second blue vertical line segment, with the lights having turned on y_{n+1} hours ago. In the upper panel, $\rho(x_n, y_n) > 24 - y_n$, therefore, the trajectory does not return to $\mathcal{P}$ within the same LD cycle. In the lower panel, $\rho(x_n, y_n) < 24 - y_n$, therefore, the trajectory does return to $\mathcal{P}$ within the same LD cycle.

3. Results.

In this section, we first show simulations demonstrating the entrainment of the strictly hierarchical CNT model. We then define and analyze a 1-D map in which O_1 is

assumed to already be entrained. We call this the O_1-entrained map. Understanding the 1-D map will facilitate the definition and analysis of the 2-D entrainment map. Finally, we extend the results to the semihierarchical case.

3.1. The entrained solutions of the CNT model. To find the entrained solutions and understand the geometry of the strictly hierarchical CNT system in the presence of the LD cycle, the nullclines of each oscillator play an important role. The nullclines are the set of points where the right-hand sides of (2) equal zero and will be different for each of the oscillators. For O_1, there are two different P-nullclines corresponding to the dark or light condition manifested through the square-wave forcing $f(t)$ and a single M-nullcline:

$$\begin{aligned} N_{P_D} &: M_1 = k_f h(P_1) + k_D P_1, \\ N_{P_L} &: M_1 = k_f h(P_1) + (k_D + k_L) P_1, \\ N_{M_1} &: M_1 = g(P_1). \end{aligned} \tag{8}$$

For O_2, there is a single P-nullcline (since $k_{L_2} = 0$), but a family of M-nullclines since the coupling from O_1 is continuous rather than discrete:

$$\begin{aligned} N_P &: M_2 = k_f h(P_2) - k_D P_2, \\ N_{M_2} &: M_2 = g(P_2) + \alpha_1 M_1 g(P_2). \end{aligned} \tag{9}$$

Each P-nullcline is a cubic shaped curve. Note that N_{P_D} and N_{P_L} are independent of the variables P_2 and M_2. In the four-dimensional space (P_1, M_1, P_2, M_2) they actually correspond to hypersurfaces. But since the equations governing the evolution of O_1 are independent of O_2, we simply project and view N_{P_D} and N_{P_L} as curves in (P_1, M_1) space (Figure 3(a)). We similarly view the sigmoidal nullcline N_{M_1} as a curve in this phase plane. We project the nullclines of O_2 onto the (P_2, M_2) space (Figure 3(c)). Note that N_{M_2} now represents a continuum of sigmoidal shaped curves that vary depending on the value of M_1. When O_1 is entrained, along its limit cycle, the M_1 value is bounded between $\min|M_1(t)|$ and $\max|M_1(t)|$. Thus N_{M_2} can oscillate between $N_M^{\min} : M_2 = g(P_2) + \alpha_1 \min|M_1(t)| g(P_2)$ and $N_M^{\max} : M_2 = g(P_2) + \alpha_1 \max|M_1(t)| g(P_2)$. We assume that any intersection between N_P and N_M occurs on the middle branch of the corresponding cubic nullclines. This will guarantee that any ensuing fixed points of the CNT system are unstable and will allow oscillations to exist.

We plot the entrained solution of the CNT by direct simulation. In our simulations, we take a specific set of parameters for (2), i.e., $\phi_1 = \phi_2 = 2.1$, $\epsilon_1 = \epsilon_2 = 0.05$, $k_D = 0.05$, $k_{L_1} = 0.05$, $k_{L_2} = 0$, $k_f = 1$, $\alpha_1 = 2$. In Figure 3(a), the periodic solutions of O_1 are presented for different light conditions. The dashed black (red) limit cycle denotes the stable solution of O_1 in DD (LL) conditions. The solid red-black limit cycle denotes the LD-entrained solution of O_1, with hourly markings shown by green open circles. We also show various nullclines and note that the M nullcline (yellow curve) is unique, but the P-nullcline (red and blue curves) varies between $M_1 = (k_D + k_L)P + k_f h(P)$ and $M_1 = k_D P + k_f h(P)$. The corresponding time courses are shown for the P_1 variable in Figure 3(b).

In Figure 3(c), we show the entrained solutions of O_2 when O_1 is in different light conditions. The color convention is the same as in Figure 3(a). Here, we note that the P-nullcline (blue curve) is unique, but the M-nullcline (red and yellow curves) varies between

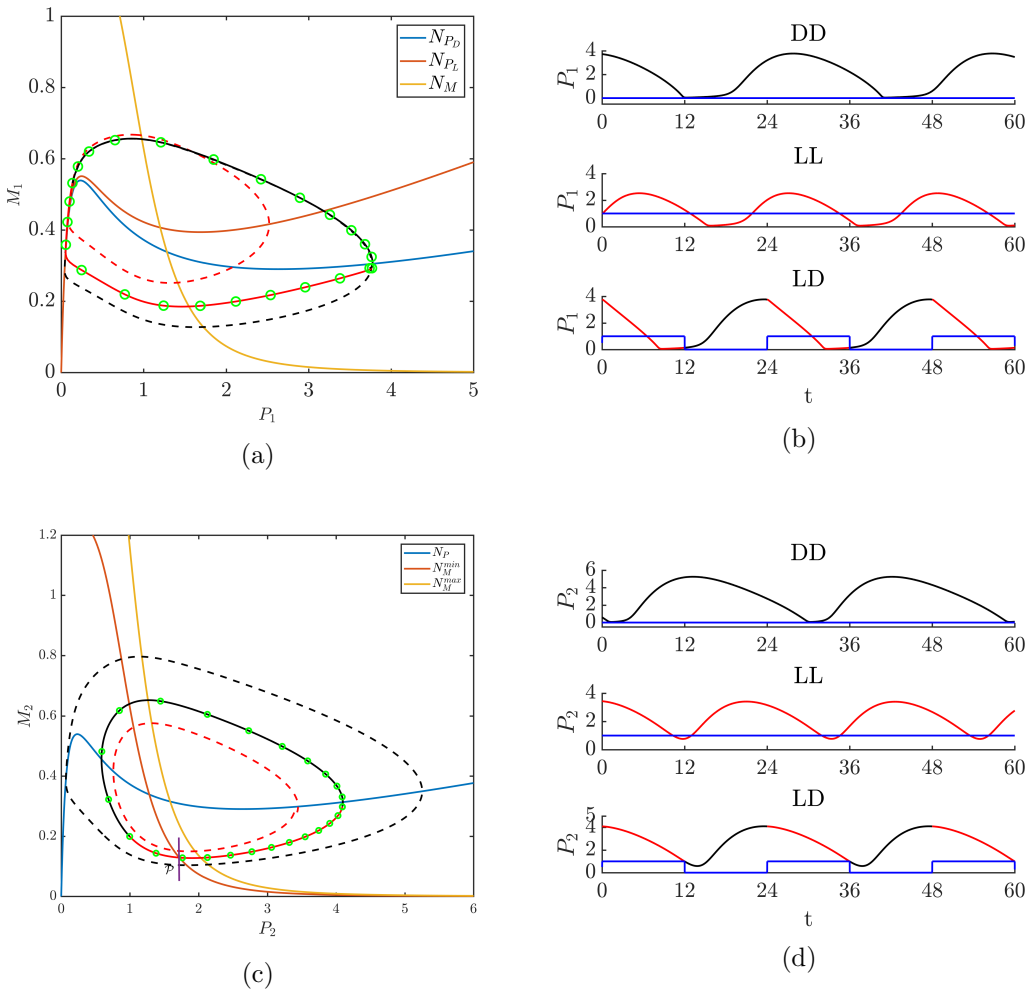

Figure 3. (a) *The periodic solutions of O_1 in DD, LL, and LD conditions. The dashed black trajectory represents the DD limit cycle ($f(t) \equiv 0$), the dashed red trajectory represents the LL limit cycle ($f(t) \equiv 1$). The solid trajectory represents the LD solution with green hourly markers. The two different P_1 nullclines, N_{P_D} and N_{P_L} and the single M_1 nullcline, N_M, are shown. Note that for panels* (a) *and* (c) *the horizontal scale is much larger than the vertical scale.* (b) *The time course plots: P_1 versus t in all three cases (blue line lies at* 0, 1, *or is a square wave for DD, LL, or LD, respectively.* (c) *The periodic solutions of O_2 when O_1 is in DD, LL, and LD conditions. Same color scheme as in* (a). *The Poincaré section is represented at $P_2 = 1.72$ by a small vertical line segment. Note that only the maximal and minimal sigmoidal M_2 nullclines, $N_M^{\min}$ and $N_M^{\max}$, are shown that bound the family of nullclines that exist for this case.* (d) *The time course plots: P_2 versus t in DD, LL, and LD conditions.*

$M_2 = (1 + \alpha_1 \min|M_1(t)|)g(P_2)$ and $M_2 = (1 + \alpha_1 \max|M_1(t)|)g(P_2)$. We also show the time course plots related to the same condition in Figure 3(d). The time course plots show that the period of the DD solution is longer than that of LD, and the period of the LL solution is shorter than that of LD. In particular, we found that the period of the DD cycle is 28.9 h, which is the same as the DD cycle of O_1, and the period of the LL cycle is 21.6 h, which

is also the same as the LL cycle of O_1. This is not surprising, because when the coupling is strong enough, O_2 is entrained by O_1.

The nullclines shown in Figure 3(c), together with the dashed LL and DD O_2 limit cycles, are useful to explain our choice of the Poincaré section at $P_2 = 1.72$, centered at $M_2 = 0.1289$. It is straightforward to use the vector field and phase plane analysis to show that any trajectory starting on $\mathcal{P}$ will evolve clockwise and cross the right branch of N_P with $P_2 > 3$. Because of the difference in scaling of the vertical and horizontal components of that phase plane it may not be so obvious that the M_2 value does not vary much for points along the right branch between where the LL (dashed red) and DD (dashed blue) limit cycles intersect it. In the LD situation, a trajectory will intersect the right branch of the N_P nullcline somewhere between a neighborhood of each of these points. We now show that any two trajectories with initial conditions lying on this nullcline in that region remain close in their M_2 value. Suppose we have a trajectory cross the right branch of N_P at $(\tilde{P}_2, \tilde{M}_2)$, where $\tilde{P}_2 > 3$, so that

$$\tilde{M}_2 = H(P_2) = k_f h(\tilde{P}_2) + k_D \tilde{P}_2.$$

Taking a derivative of the function on the right-hand side and, for convenience, using x to represent the P_2 variable, yields

$$H'(x) = k_f h'(x) + k_D = k_f \frac{0.1 - x^2}{(0.1 + x + x^2)^2} + k_D.$$

When x is large, $H'(x) \to k_D$, implying $H(x) \approx k_D x$, where k_D is a small parameter. So when $\tilde{P}_2 > 3$,

$$H(x_1) - H(x_2) \approx k_D(x_1 - x_2).$$

Thus the difference of M_2 between two points on the right branch of N_P is small. Next we show that those points have approximately the same dynamics in the M_2 direction. When P_2 is large, $g(P_2) \to 0$, the second equation of (4) is approximately

$$\frac{dM_2}{dt} = -\phi_2 \epsilon M_2,$$
$$M_2(t) = \tilde{M}_2 e^{-\phi_2 \epsilon t}.$$

The main point here is that the effect of M_1 is gone, so trajectories evolve largely independent of the coupling. Since any initial points lying on the region of the right branch of the N_P nullcline are close in their M_2 value, it is an easy application of Gronwall's inequality to show that they remain close until P_2 becomes sufficiently smaller. Thus those trajectories are funneled into the small region between the LL and DD limit cycles and cross the Poincaré section.

We note that our choice of Poincaré section is dictated by the funneling effect. For example, choosing the section elsewhere, say $P_2 = 3$, $|M_2 - 0.521| < \delta$, $\delta > 0$ but small, would not guarantee that trajectories cross through this section again. Trajectories will, of course, cross $P_2 = 3$ with $P_2' > 0$, but won't necessarily do so in a small neighborhood of the LD-entrained solution.

3.2. The O_1-entrained map. The O_1-entrained map we obtained from (5) has similar properties as the entrainment map Diekman and Bose constructed in their paper [13]. Figure 4 shows that there are two fixed points which correspond to different types of periodic solutions for the CNT system. The lower one with $y_{n+1} = y_n = 10.2$ is a stable fixed point of the map, which represents a stable periodic solution. The upper one with $y_{n+1} = y_n = 17.2$ is an unstable fixed point of the map.

We classify the direction of entrainment as occurring through phase advance or phase delay. Suppose $y_{n+1} = \Pi_{O_1}(y_n)$, and the return time needed from y_n to y_{n+1} is less than 24 hours. We call this a phase advance. Alternatively, if the return time is greater than 24 hours, we call it a phase delay. The unstable fixed point of the map plays an important role in determining this direction. For example, pick two different initial conditions ($y_0 = 16.5, 18$) near the unstable fixed point and use the cobweb method to observe how different directions of entrainment can occur. For $y_0 = 16.5$, the iterates move to the left and converge to the stable solution by phase advance. For $y_0 = 18$, however, the iterates move to the right and converge to the stable solution by phase delay. In Figure 4(b), we compare the iterates with simulations; the green curve corresponds to $y_0 = 16.5$ and the magenta curve corresponds to $y_0 = 18$. The black curve is the entrained solution for O_2. The direction of entrainment from the simulations agrees with the calculations obtained from the map.

In our model system, there are two parameters of interest, the coupling strength α_1 and the intrinsic period of O_2 governed by ϕ_2. In Figure 4(c), we decrease α_1 from 2.5 to 1.4, so that the coupling strength is weaker. As a result, the return time $\rho(y)$ increases. This makes the map move up, and the stable and unstable fixed points get closer to each other. At $\alpha_1 = 1.51$, the two fixed points collide at a saddle-node bifurcation. In Figure 4(d), we increase the intrinsic period of O_2 by decreasing ϕ_2 from 2.3 to 1.9, so that the difference between the intrinsic period and the 24-h forcing increases, which increases the return time to the Poincaré section. Hence the map moves up. When $\phi_2 = 1.91$, the map passes through the saddle-node bifurcation value. The disappearance of the stable fixed point means that in the full system 1:1 entrainment is lost and replaced by higher order periodic behavior. The details of this kind of behavior are interesting in their own right, but an investigation of this behavior is beyond the scope of this work.

Notice that the O_1-entrained map we construct is not monotonic, which makes it different from the 1-D entrainment map found in [13]. To understand this nonmonotonicity, we take two initial conditions ($y_0 = 6$ and $y_0 = 8$) near the local maximum of the map in Figure 5(a), and analyze the dynamics of the system. Associated with the return time plot in Figure 5(b), we found that the return time is between 28 and 29 when y is less than the local maximum point. But when it crosses that point, the return time decreases quickly with the derivative $\rho'(y) < -1$. In Figure 5(c), we plot the trajectories with the two initial conditions. The trajectory for $y_0 = 6$ flows to the left branch of the P-nullcline, which increases the return time since evolution near this branch is slow. Alternatively, the trajectory for $y_0 = 8$ doesn't flow near the left branch and thus has a shorter return time. A minor consequence of this nonmonotonicity is that some solutions converge to the stable fixed point by initially phase delaying, but then ultimately phase advancing. For example, in Figure 5(d), we take $y_0 = 18$ then cobweb the map. We find that the first four iterates initially phase delay. The fourth iterate lands near the local maximum of the map, which lies above the value of the fixed point.

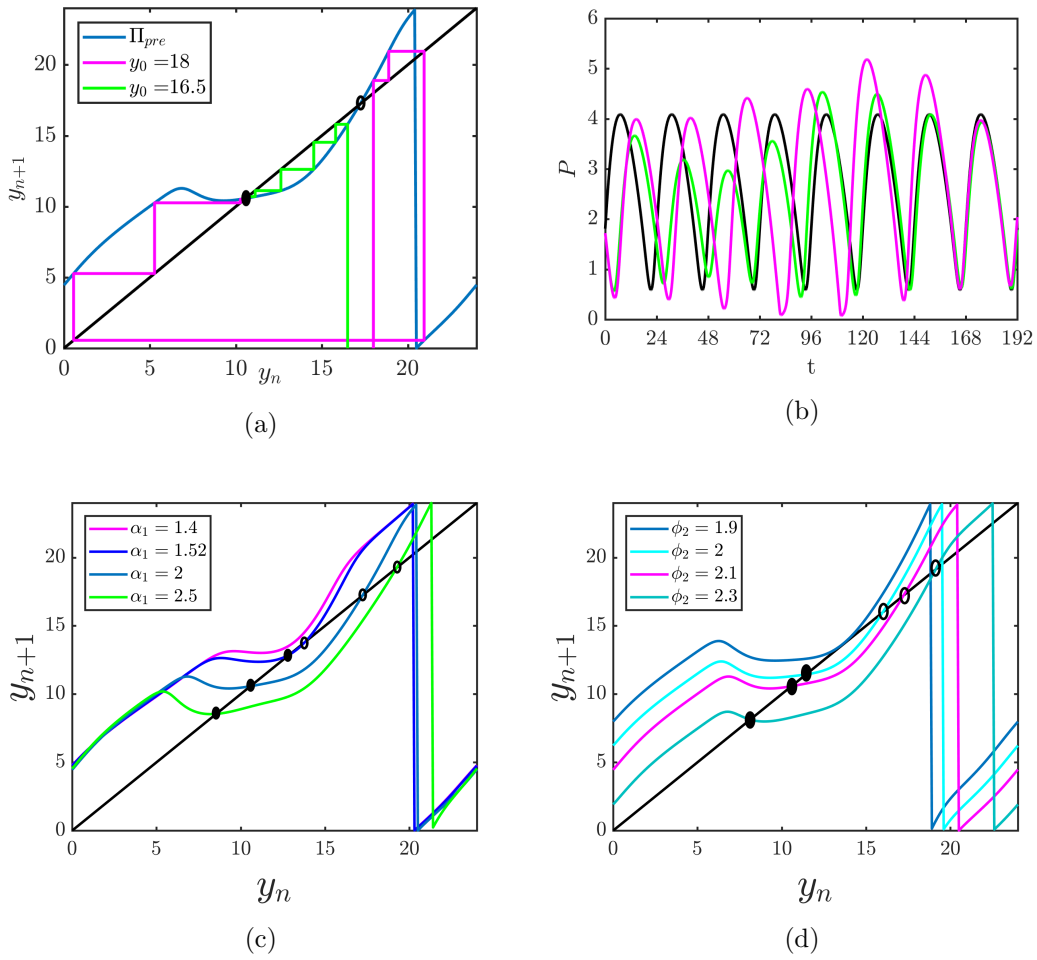

Figure 4. (a) *The cobweb diagram for the O_1-entrained map. We pick two different initial conditions and show how the iterates move to the stable fixed point.* (b) *The approach to the stable solution (black curve) in the t versus P plane; the colors correspond to the two initial conditions in* (a). (c) *The map displays a saddle-node bifurcation by decreasing α_1.* (d) *Decreasing the intrinsic period of O_2 by decreasing ϕ_2 also leads the map to display a saddle-node bifurcation. Fixed points shown as open circles are unstable, and those shown with solid circles are stable.*

This causes subsequent iterates to phase advance. This nonmonotonicity foreshadows a more complicated picture that arises under the dynamics of the 2-D map.

3.3. The results of the general 2-D map. In this section, the analysis of the 2-D map is presented. We follow ideas first derived by Akcay, Bose, and Nadim [1] and followed up on in [2] to find fixed points of the map via a geometric method. The entrainment time and the direction of entrainment are analyzed by iterating the map. We also compare these results with simulations. At the end of this section, we show that the map is also applicable to the semihierarchical model.

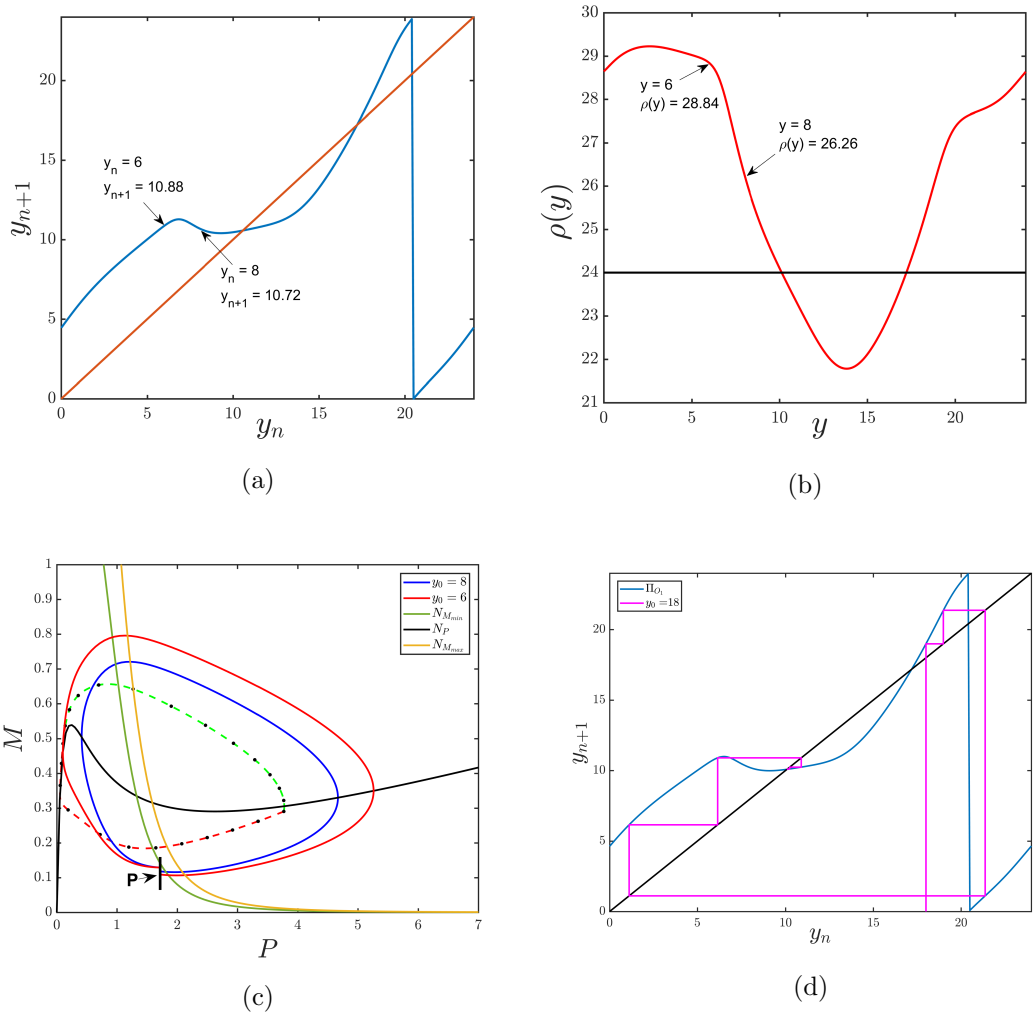

Figure 5. *Nonmonotonicity in the entrainment map leads to convergence initially due to phase delay but ultimately due to phase advance.* (a) *The nonmonotone O_1-entrained map and two choices of initial conditions near the local maximum. Note that the local maximum lies above the value of the fixed point of the map.* (b) *The return time plot associated with the two initial conditions.* (c) *The corresponding phase plane. The solid blue trajectory for $y_0 = 8$ does not approach the left branch of N_P, while the solid red trajectory for $y_0 = 6$ does, causing its evolution to slow down.* (d) *Starting with an initial condition $y_0 = 18$, the first four iterates phase delay. The fourth iterate lands near the local max of the map, and subsequent iterates then phase advance.*

Basic results from the map. Both parts of the 2-D map Π_1 and Π_2 are surfaces in relevant 3-D spaces. Because of the mod 24 operation, each surface will contain discontinuities. In Figures 6(a) and 6(b), we project the surface onto the x–y plane. For Π_1, the purple part of the surface is points lying above the diagonal plane $z = x$, in other words, $x_{n+1} > x_n$. The red part of the surface of Π_2 is points lying above the diagonal plane $z = y$, i.e., $y_{n+1} > y_n$. The points of gray color denote all points that are below the diagonal planes, $x_{n+1} < x_n$ and

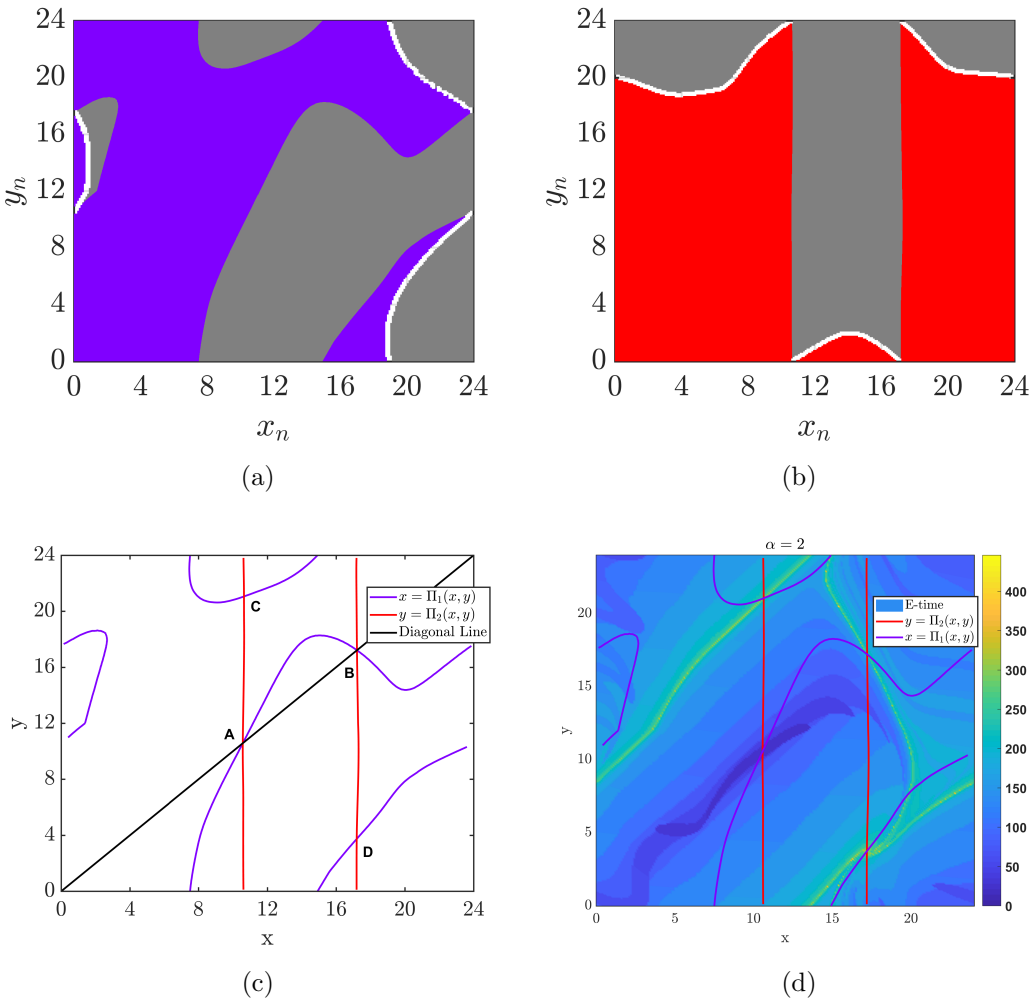

Figure 6. (a) *and* (b) *The* 2*-D entrainment map is plotted as two separate maps* Π_1 *and* Π_2*, and projected onto the domain space* (x_n, y_n)*. The purple and red color in both maps denote all points that are above the diagonal plane. The gray color denotes points that are below the diagonal plane. The white curves denote the discontinuity.* (c) *The purple curves denote points of* Π_1*'s nullcline* N_x*, where* $x = \Pi_1(x, y)$*, the red curves denote points of* Π_2*'s nullcline* N_y*, where* $y = \Pi_2(x, y)$*. Their intersections are the four fixed points of the map.* (d) *The entrainment time is plotted with a heatmap. The color denotes the entrainment time starting from a specific initial condition. The light green curves locate* $W^s(B)$ *and* $W^s(C)$ *from near which the longest entrainment times occur.*

$y_{n+1} < y_n$. The white curves indicate locations of discontinuity of the map. The separation of the two different colors consists of curves which indicate the points where $x = \Pi_1(x, y)$ and $y = \Pi_2(x, y)$. Here we define those curves as nullclines of the map:

$$N_x = \{(x, y) : x = \Pi_1(x, y)\}, \quad N_y = \{(x, y) : y = \Pi_2(x, y)\},$$

which are plotted in Figure 6(c). The purple curves denote N_x. Similarly, the red curves

Table 1

Numerical computation of the eigenvalues of the map at the four fixed points. Eigenvalues with modulus less than one correspond to stable directions, while those with modulus greater than one correspond to unstable directions.

	x	y	Eigenvalue	Stability
A	10.6	10.6	0.1609, 0.4453	sink
B	17.2	17.2	2.0858, 0.4238	saddle
C	10.6	21.1	2.325, 0.2734	saddle
D	17.2	3.7	1.595+0.77i, 1.595-0.77i	source

denote N_y. Their intersections are four fixed points of the map. We numerically calculated the Jacobian at those fixed points and found the eigenvalues of the linearization. These values and the corresponding stability of each fixed point are shown in Table 1. From the results of the O_1-entrained map, points A and B lying on the diagonal line correspond to the stable solution of O_1. For O_2, point A corresponds to the stable solution. For point B, the trajectory of O_2 returns to the Poincaré section after 24 hours but corresponds to the unstable solution of the O_1-entrained map. At the fixed point C, O_1 lies on its own unstable periodic orbit. This can be inferred from and agrees with the calculation of Diekman and Bose [13] who showed that the original 1-D entrainment map has an unstable fixed point that corresponds to an unstable periodic orbit. Thus O_1 is entrained to a 24-hour LD cycle and provides a 24-hour forcing to O_2. From simulation, we found that the trajectory of O_2 stays for several cycles near what appears to be a stable limit cycle, though it is different from the limit cycle corresponding to point A since O_1 is unstable and the forcing signal to O_2 is different. At point D, if we check the difference between C and D, we can see that

$$(x_D, y_D) = (x_C, y_C) + 6.6 \bmod 24,$$

so O_1 is still on its unstable periodic orbit. That is, points C and D represent conditions where the forcing $M_1(t)$ is identical, but just phase shifted by 6.6 hours. Thus O_2 still receives 24-hour forcing so we also expect there to exist an unstable O_2 limit cycle for this case.

One advantage of the map is its ability to estimate the entrainment time. Starting from different initial conditions, we iterate the map $(x_{n+1}, y_{n+1}) = \Pi(x_n, y_n)$ until $\|(x_{n+1}, y_{n+1}) - (x_s, y_s)\| < 0.5$, where point A has coordinates (x_s, y_s). The entrainment time is the sum of the return times corresponding to each iterate. In Figure 6(d), we show the entrainment times corresponding to different initial conditions on the torus expanded as a square. We also plot the nullclines N_x and N_y on top of it for illustrative purposes. The color for each point on the square denotes the entrainment time needed for that initial point.

Notice that, in Figure 6(d), there are two light green curves. Along these curves, the entrainment time is much longer than other regions. Additionally, they appear to connect the two saddle points B, C with the unstable source D. Though not proven here, we believe that these curves locate where the stable manifolds of the saddle points B and C ($W^s(B)$ and $W^s(C)$) are. To completely understand the dynamics of the entrainment map, it is useful to numerically find the stable and unstable manifolds.

The algorithm we used to find the manifolds of the entrainment map are based on the following results. For the unstable manifold, Krauskopf and Osinga [26] introduced a growing

method to calculate the unstable manifold point by point. They initially iterate points chosen in a neighborhood of the fixed point along the associated unstable eigenvector and accept new points as lying on the unstable manifold if they satisfy specific constraints. For the stable manifold, the search circle (SC) method introduced by England, Krauskopf, and Osinga [16] utilizes the stable eigenvector to find points within a certain radius that iterate onto a segment of the stable eigenvector. The SC method has the advantage that it does not require the inverse of the map to exist, which is important for us since our map is noninvertible. Both of these methods are constructed for planar nonperiodic domains. In our case, the map lives on a torus, but is graphically shown on a square. Whenever an iterated point exceeds the boundary of the square, we use the modulus operation to define the correct value within the square. Thus we develop our algorithm to account for this discontinuity. Another difference is that the terminating conditions for both the growing and SC methods rely on calculating the arc length of the manifolds up to a certain predetermined length. However, in our map, the stable manifolds of points B and C are generated from the source point D, while their unstable manifolds terminate at point A. Thus our algorithm terminates when these manifolds enter prescribed neighborhoods of those corresponding fixed points D and A.

In Figure 7(a), we choose initial points ranging from $0 < x < 24, 0 < y < 24$, and iterate ten times for each initial point. The arrow on each coordinate is pointing to its own next iterate. The obtained vector field give us another visualization of the map. In Figure 7(b), the numerical result of stable and unstable manifolds of B and C are plotted (also overlayed in panel (a) for easier comparison). $W^s(B)$ and $W^s(C)$ agree with the light green curves in Figure 6(d). $W^u(B)$ is exactly the diagonal line of the phase plane, which is not surprising. Because the diagonal line corresponds to the O_1-entrained case, if an iterate starts on the diagonal line, it stays on it. The numerical calculation of the eigenvector of $E^u(B)$ is approximately (0.7,0.7) on the diagonal line, which means $W^u(B) = E^u(B)$. $W^u(C)$ also matches the darkest region in Figure 7(a). Indeed, these dark regions indicate the location of the unstable manifolds of points B and C. The located manifolds are also helpful for understanding the direction of entrainment of 2-D maps. In the case of the 1-D map, the direction of entrainment is essentially either phase advance or delay, and the longest entrainment times happen for initial conditions lying near the unstable fixed point. In the case of the 2-D map, the direction of entrainment need no longer be monotonic. The manifolds associated with the saddle points B and C appear to behave like a separatrix, despite this being a map and not a flow. To classify the direction of entrainment in the 2-D map, we consider phase delays and advances in the x and y directions separately. For the x direction, if the rotated angle from x_n to x_{n+1} is greater than 2π, we call it phase delay, otherwise we call it phase advance. For the y direction, we use the same definition as in the O_1-entrained map. To illustrate different directions of entrainment, we pick several initial conditions near the stable manifolds, then iterate the map. We also run simulations with the same initial conditions for comparison. For Figure 8(a), in the left panel, we pick an initial point slightly above $W^s(C)$. It entrains to the stable solution by phase delay in the y direction, and phase delay-advance-delay in the x direction. In the right panel, the initial point is slightly below $W^s(C)$, but the entrainment is through phase delay-advance in y, and phase delay-advance in x. The corresponding simulations in Figure 8(b) agree with the direction of entrainment found through the map and demonstrate the sensitivity to initial conditions.

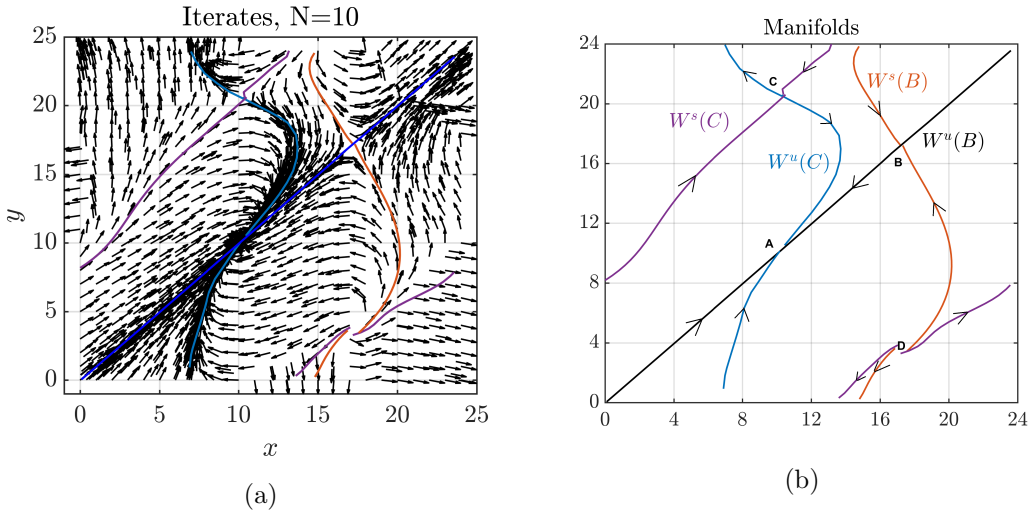

Figure 7. (a) $N = 10$ *iterates from various initial points are shown. The arrow at each coordinate point is in the direction of the next iterate. The vector field indicates that there may exist a separatrix type structure at both points B and C.* (b) *Stable and unstable manifolds of B and C as generated through the generalization of the search circle and growing methods (see text) which are also overlayed in panel* (a). *The labeled manifolds do appear to provide a separatrix type behavior despite this being a map and not a flow.*

Parameter dependence of the map. In the section on the O_1-entrained map, we calculated the O_1-entrained map for four different values of α_1, and found the system will lose entrainment if the coupling strength is too small. Now we calculate the 2-D map at different values of α_1 to see how the fixed points and the entrainment time depend on α_1. In Figures 9(a) and 9(b), we show the x and y nullclines for three different α_1 values; the points with a a solid circle are the stable fixed points, the points with open circles are the unstable fixed points, and the starred points are saddle points. In Figure 9(c), we show the heatmap of entrainment times for $\alpha_1 = 1.52$. In Figures 9(d), we show the heatmap of entrainment times for $\alpha_1 = 2.5$. Note that $\alpha_1 = 2$ is our canonical case, and was presented before in Figure 6(d). Increasing α_1, in general, decreases the entrainment time as can be observed from the color scale values (yellow max value ≈ 700 for $\alpha_1 = 1.52$) versus 400 for $\alpha_1 = 2.5$. In other words, stronger coupling between the central to peripheral oscillator speeds up entrainment.

The 2-D map for the semihierarchical case. For the strictly hierarchical model with only one feedforward connection from O_1 to O_2, we have shown how to construct both the O_1-entrained map and the general 2-D entrainment map. Here we will show that the 2-D map can be derived for the model when $0 < k_{L_2} < k_{L_1}$. In this case, O_1 is still dominant, allowing us to keep a semihierarchical structure.

We take $k_{L_2} = 0.025$, and keep the values of other parameters the same, so that O_1 and O_2 both receive light forcing. We define the Poincaré section $\mathcal{P} : P_2 = 1.72, |M_2 - 0.1548| < \delta$. We then obtained a 2-D map for this model. In Figures 10(a) and 10(b), the top view of Π_1 and Π_2 are presented. In Figure 10(c), we similarly obtained 4 fixed points (A,B,C,D) as in the strictly hierarchical case. Compared to the strictly hierarchical model, we found that the additional light forcing into O_2 accelerates the entrainment process, so that the time to

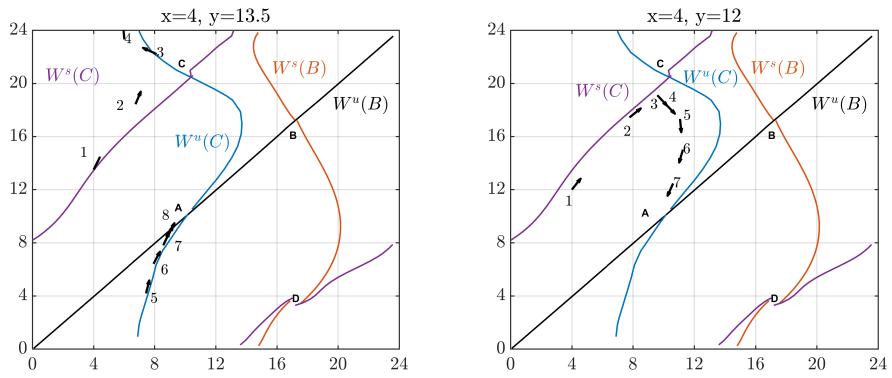

(a)

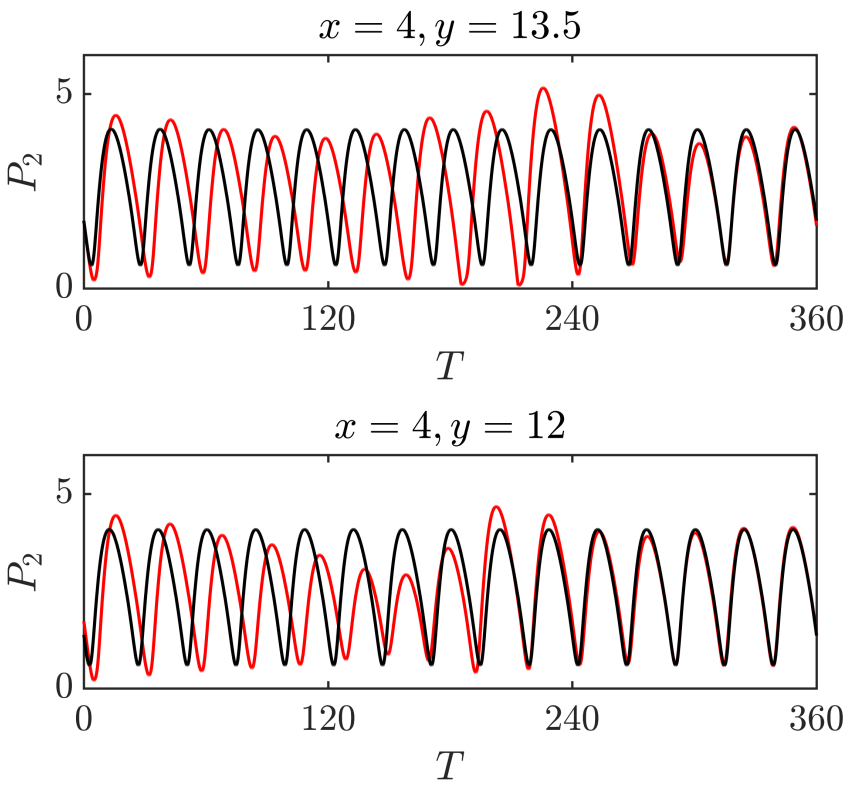

(b)

Figure 8. *Direction of entrainment depends sensitively on initial conditions.* (a) *The initial point (labeled* 1*) in the left panel lies above* $W^s(C)$*, while the similarly labeled point in the panel to the right lies below* $W^s(C)$*. Numbers indicate iterates. As shown, the direction of entrainment differs significantly.* (b) *Corresponding simulations agree with the iterates. Note the top panel shows that* O_2 *(red time course) entrains through phase delay to the entrained solution (black time course); the lower panel shows* O_2 *entraining through phase delay-advance.*

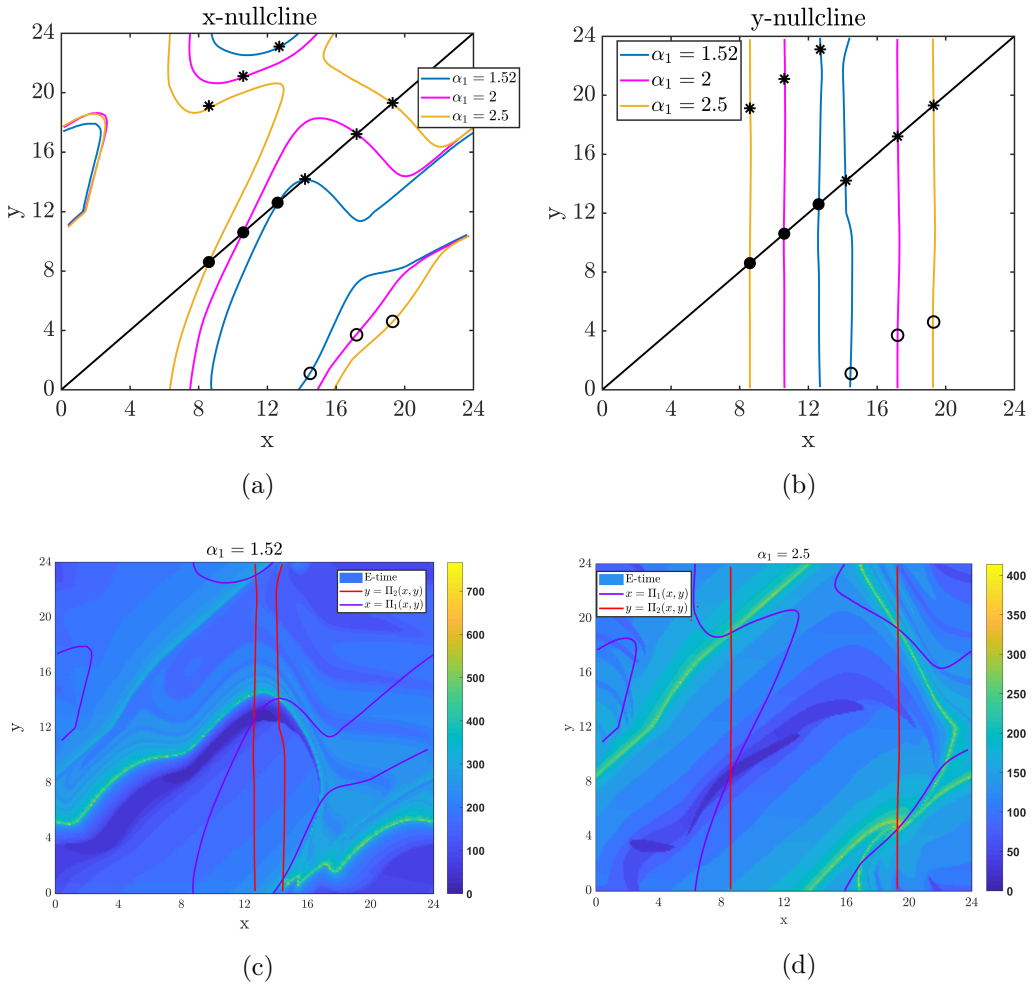

Figure 9. (a)–(b) *The x and y nullclines under different α_1 values. Solid circles denote stable fixed points, open circles unstable fixed points, and stars saddle points.* (c)–(d) *The heatmap of entrainment times for different values of α_1. Note the difference in numeric value of the maximum value of the color scale.*

return to $\mathcal{P}$ is decreased. Thus the whole surface shifts down, which causes A to move to the left of the diagonal, and B to move to the right of the diagonal. For points C and D, the limit cycle of O_2 is now determined by both O_1 and the light forcing, which changes the location of C and D. In Figure 10(d), we calculated the first 10 iterates of each initial point. Comparing these results with the strictly hierarchical case, the stability of each fixed point remains unchanged, but their location has changed. Further, the entrainment time required for each initial condition is reduced because of the LD forcing into O_2.

4. Discussion. Circadian oscillations exist from the subcellular level involving genes, proteins, and mRNA up to whole body variations in core body temperature. These oscillations are typically entrained to the 24-hour LD cycle. Additionally, food, exercise, exterior temperature, and social interactions can also act as entraining agents in certain species [34]. In

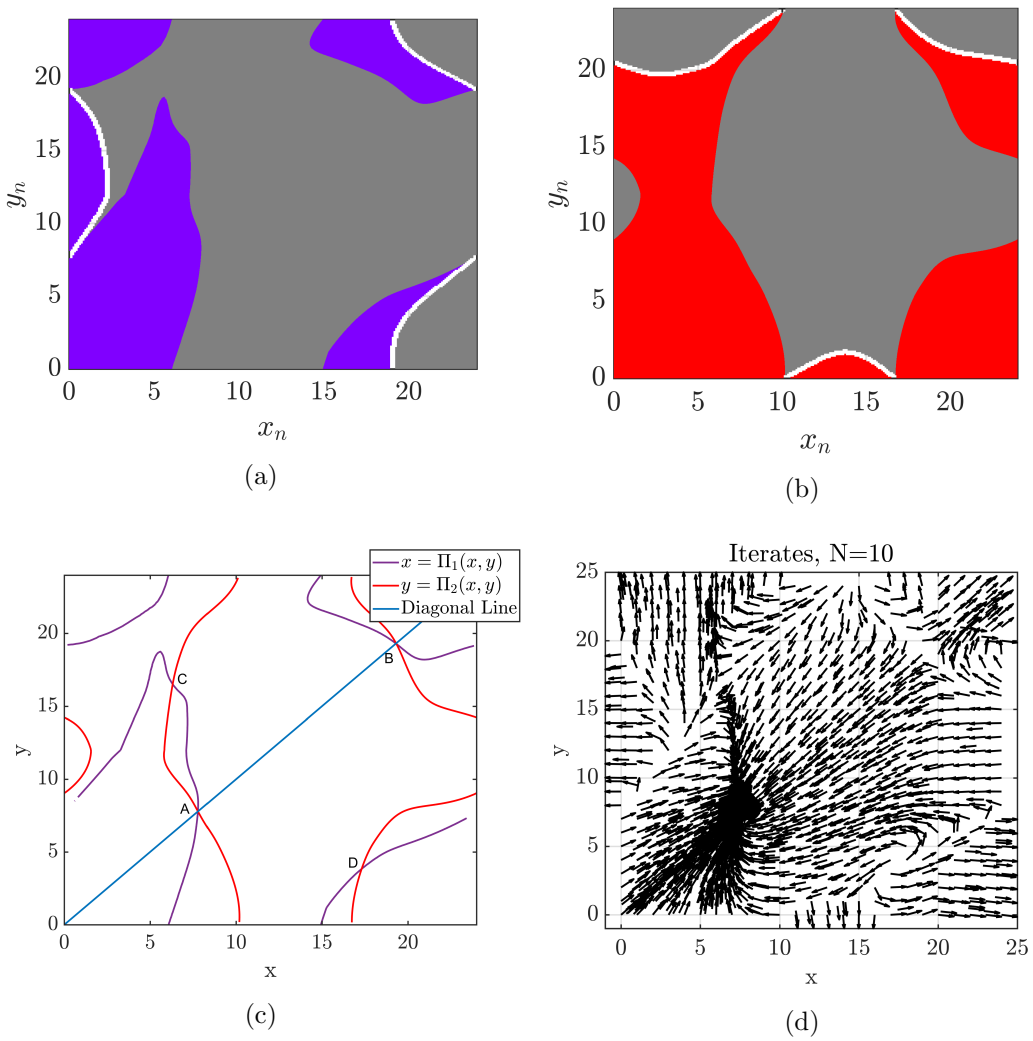

Figure 10. 2-*D semihierarchical case.* (a)–(b) *The top view of* Π_1 *and* Π_2 *are presented; see Figures* 6(a) *and* 6(b) *for an explanation of color coding.* (c) *We obtained* 4 *fixed points (A,B,C,D) with similar stability of the canonical model.* (d) *Ten iterates of each point. The vector field looks qualitatively similar to the strictly hierarchical case shown in Figure* 7(a).

these cases, various pathways in each species exist which carry the entraining information to relevant parts of the circadian system. In this paper, we refer to the set of oscillators that first receive this input as central circadian oscillators. In turn, these central oscillators send signals about the time of day to other peripheral oscillators. When viewed in this manner, we obtain a hierarchical circadian system. For example, in the strictly hierarchical model (Figure 1(a)), the central oscillator O_1 could represent the suprachiasmatic nucleus (SCN), the master pacemaker in the hypothalamus of mammals. The peripheral oscillator O_2 that does not receive light input could represent circadian clocks in organs such as the heart or

kidney. Alternatively, O_1 could represent the part of the SCN that directly receives light input (the ventral core), and O_2 could then represent the part of the SCN that does not (the dorsal shell) [21]. For the semihierarchical model (Figure 1(b)), O_1 and O_2 could represent the central and peripheral clocks in *Drosophila*, since in flies the clock protein cryptochrome is a photoreceptor and thus even peripheral organs receive some direct light input [11]. The main goal of this paper has been to develop a low-dimensional method to study the basic properties of hierarchical systems such as the existence and stability of entrained solutions, together with how the phase and direction of entrainment of the constituent oscillators depend on important parameters.

In this work, we have focused on how a hierarchical circadian system entrains to an external 24-hour LD cycle. To do so, we developed a method, partly analytic and partly computational, to assess the existence and stability of the entrained solution. Generalizing the approach of Diekman and Bose [13], we derived a Poincaré map by placing a section in the phase space of the peripheral oscillator O_2. The phase of O_1 with respect to a reference point on its own limit cycle, x, and of lights y, was then determined to derive the 2-D map. With this approach, we were able to determine that over a large set of parameters, the 2-D map possesses four fixed points, each of which corresponds to a periodic orbit of the hierarchical circadian system. Only one of these fixed points is asymptotically stable. The other three fixed points are unstable. We showed how one of them, labeled D in Figures 6(c), 7(b), and 10(c), is a source from which iterates emerge, including the stable manifolds of the two saddle points B and C. These manifolds appear to act as separatrices in the x-y domain of the map in the sense that, although they are for a map and not a flow, the manifolds separate the direction of convergence towards the stable fixed point A. Perhaps this is not so surprising as the saddle structure of the fixed points implies the existence of a saddle structure of the periodic orbits associated with points B and C. In the full 5-D phase space of the flow, each of the corresponding 1-D stable and unstable manifolds from the map become 3-D; the motion along the O_1 and O_2 limit cycles provide the additional two dimensions. This would be enough to form a separatrix in the 5-D phase space.

There are several findings of our work that are readily revealed through the 2-D map. First, in a strictly hierarchical system, central oscillators typically entrain first. This can be seen quite clearly from Figure 7(a) which shows that iterates of the map congregate along the diagonal line, which represents the O_1-entrained subset of the 2-D map. This figure also shows that the peripheral oscillators may entrain in a different direction than the central oscillator or may in fact change their direction of entrainment during the transient. Given that direct light input speeds up entrainment, it is intuitively clear to see why entrainment times are, in general, less for semihierarchical compared to strictly hierarchical systems; see Figure 10. A second finding involves the stable and unstable manifolds of the fixed points. Despite this being a map, these manifolds help to organize the iterate structure. In particular, the stable manifolds of the unstable saddle points create a tubular neighborhood of initial conditions that lead to very long entrainment times, as seen in Figure 6(d). Determining that the unstable node and saddle points of the map actually exist is yet another important consequence of our map-based approach. Simulations alone would be unlikely to reveal either the existence or the role of these fixed points. Finally, effects of changing relevant parameters are readily explained

using the map. For example, the limits on parameters of entrainment are readily observed if the coupling to the peripheral oscillator is too weak or if that oscillator is intrinsically too slow (Figure 4). Alternatively, stronger coupling from central to peripheral oscillators speeds up entrainment as shown in Figure 9.

Related work. The mechanisms of communication between clock neurons is a topic of much ongoing research in the circadian field. The neuropeptide pigment-dispersing factor (PDF) is thought to act as the main synchronizing agent in the fly circadian neural network [32]. The analogue of PDF in the mammalian circadian system is vasoactive intestinal peptide (VIP), which plays a major role in synchronizing SCN neurons [33]. Although it is clear from studies with mutants that these neuropeptides provide important signals to synchronize circadian cells, the manner in which the signals interact with the molecular clock is not well understood [15]. Mathematical modeling can be used to explore the effect of different coupling mechanisms on clock network synchronization. In our model, we have assumed that production of the synchronizing factor is induced by activation of the clock gene in oscillator 1 (M_1), and that the effect of the synchronizing factor is to directly increase transcription of the clock gene in oscillator 2 (M_2). This type of coupling is similar to how Gonze et al. [18] modeled the action of VIP in the mammalian clock network; however, in the Gonze model they included a linear differential equation for the production and decay of the coupling agent. Thus, in their model the coupling agent is a delayed version of the clock gene activity. In the Roberts et al. [39] model of the fly clock network, the coupling signal is also increased by clock gene activity. As in our model, the coupling signal then instantaneously increases the clock gene transcription rate in other oscillators. In addition, the Roberts model included a second type of coupling where the coupling signal depends on clock protein levels, rather than clock gene activity, and the effect of the coupling signal is to instantaneously reduce the clock gene transcription rate in other oscillators. Their simulations suggested that networks with both coupling types promoted synchrony and entrainment better than networks with either type of coupling alone. In a more detailed model of the fly clock network, Risau-Gusman and Gleiser [38] explored 21 different coupling mechanisms and found that synchronization of the network can only be achieved with a few of them. In future work, it would be interesting to use generalized entrainment maps to try to gain insight into why certain types of coupling promote synchrony and entrainment better than others.

Several prior modeling studies on entrainment of circadian oscillators exist. Bordyugov et al. [7] used the Kuramoto phase model and found, via Arnold tongue analysis, that the forcing strength and the oscillator amplitude both affect the entrainment speed. As noted in their work, a limitation of the method is that it only works for relatively weak coupling. An et al. [3] found that large doses of VIP reduce the synchrony in the SCN, which then reduces the amplitude of circadian rhythms in the SCN. In turn, they show that this leads to faster reentrainment of the oscillators in a jet lag scenario. Lee et al. [28] directly introduced a linear phase model to study the entrainment processes. They found that the period of the central and peripheral oscillators are not the only predictors of the entrained phase. The intensity of light forcing to the central oscillator and the strength of coupling from the central to the peripheral oscillator also play a role in determining the stable phase. Their results are consistent with what we found for the O_1-entrained map shown in Figure 4. Roberts et al. [39] studied a population of coupled, modified, heterogeneous Goodwin oscillators under DD

and single light pulse conditions. Their model simulations of a semihierarchical system show that because of heterogeneity, a single light pulse can desynchronize and phase disperse the oscillators. This can lead to a change in the coupling strength between oscillators which in turn leads to a new periodic solution of different amplitude than before the light pulse. Although they didn't consider 24-hour LD forcing, Roberts et al. suggests that this desynchrony can be an important component in assessing reentrainment of semihierarchical networks after jet lag. Our 2-D entrainment shows that this is indeed true. Namely, a shift in the light phasing that retains synchrony between O_1 and O_2 is equivalent to changing the initial y-value of our map, but keeping x fixed. Whereas a shift of light phasing accompanied by a desynchronization is equivalent to changing both x and y from the stable fixed point. As our simulations show (Figure 10(d)), the reentrainment process can be quite different in these two cases.

There are two modeling papers of hierarchical systems that are quite relevant to our work. In Leise and Siegelman [29], the authors consider a multistage hierarchical system to assess properties of jet lag. They utilized a 2-D circadian model due to olde Scheper et al. [37] to show that the direction of entrainment of peripheral oscillators need not follow that of the central oscillator. This is referred to as reentrainment by partition. To understand this idea more clearly, consider the concepts of orthodromic and antidromic reentrainment which are studied in the context of a time zone shift as in jet lag. Orthodromic reentrainment is defined as the oscillator shifting in the same direction as the forcing signal (e.g., advancing in response to an advance of the LD cycle) and antidromic reentrainment is when the oscillator shifts in the opposite direction as the forcing signal (e.g., delaying in response to an advance of the LD cycle). The situation is more complicated for hierarchical systems where different parts of the system may shift in different directions. For example, when Leise and Siegelman simulated a jet lag scenario involving a phase advance of 6 hours, they found that the pacemaker oscillator responded by phase advancing but the intermediate and peripheral oscillators responded by phase delaying. Similarly to Leise and Siegelman, we also observe reentrainment by partition in our model. With the parameter values that we used in this paper, a 6-hour phase advance leads to orthodromic reentrainment in our model with both oscillators responding by phase advancing. However, simulating a 10-hour phase delay of the LD cycle places the initial condition in the vicinity of the saddle fixed point C, leading to reeentrainment through partition depending on the exact location relative to C. Our results are consistent with those of Leise and Siegelman, as they note that in their model reentrainment by partition can also be observed in response to phase delays of the LD cycle for certain values of the coupling strength between the master pacemaker and the intermediate component. The qualitative similarity in our results suggests that our findings can be used to infer that the Leise-Siegelman multistage model also possesses unstable saddle fixed points whose properties govern the reentrainment process. A second more recent paper due to Kori, Yamaguchi, and Okamura [24] developed a hierarchical Kuramoto model to study the entrainment of circadian systems. They applied the model to predict the reentrainment time after two types of phase shifts, a single eight-hour shift versus a two-step shift with 4-hour shifts in each step. It turns out the latter requires fewer days to recover. In our paper, this can be related to the properties of stable manifolds of B or C. For example, in Figure 6(d), for a single eight-hour shift near the fixed point A, the new point will stay close to $W^s(C)$, which makes the reentrainment time longer. For two successive four-hour shifts,

the new point will be further from $W^s(C)$, which decreases the reentrainment time. This result generalizes findings from Diekman and Bose [14] and Kori, Yamaguchi, and Okamura [24].

Regarding the numerical methods that we used to find stable and unstable manifolds, we basically applied the search circle for stable manifolds [16] and the growing method [26] for unstable manifolds. One difference between those methods and ours is the domain of the map, $\mathbb{R}^2$ versus a torus $\mathbb{T}^2$ in our case. Instead of growing one curve, our manifold is cut off when it hits the boundary of the domain. We then restart the calculation at the equivalent periodic point of the domain, e.g., $x = 24$ is reset to $x = 0$. Another difference is the terminating criteria for both growing and SC methods rely on calculating the arc length to a predetermined length. However, in our map, the manifolds are generated from a certain point (the source D or the sink A), thus our algorithm terminates when those manifolds enter a neighborhood of the corresponding fixed points D and A.

Recently Castejón and Guillamon derived a different 2-D entrainment map [9]. This map applies to a single oscillator (not necessarily a circadian oscillator), subject to pulsed periodic input. The variables of their map are the phase and amplitude of the oscillator. They use phase-response curve type methods to show that their 2-D map is more accurate in tracking the phase-locking dynamics as compared to a 1-D map of simply phase. While they use the term 2-D entrainment map, it appears that their method applies to a class of problems that are different than the ones considered in this paper.

Advantages and disadvantages of our method. The methods derived in this paper have the following advantages. Aside from allowing us to calculate entrainment times and directions as discussed above, the method provides a clear geometric description of why these results arise. Namely, the unstable manifolds of various fixed points organize the iterate structure of the dynamics. Our method does not specifically require the LD forcing to be weak in amplitude or short in duration. This is in contrast to methods that use phase response curves and thus require weak coupling or short duration perturbations [8, 35].

Second, the dimension on which we perform analysis is significantly reduced from five to two dimensions. The classical Poincaré map can reduce the dimension of the original system by one. For example, Tsumoto et al. [40] construct a Poincaré map for the 10-dimensional Leloup and Goldbeter model of the *Drosophila* molecular clock [30], reducing the dimension to 9. The phase reduction techniques of Brown, Moehlis, and Holmes [8] can reduce the dimension of limit cycle oscillators to 1 dimension, however, this method is not accurate for strong coupling.

There are some disadvantages of the map. First, the map only works to study local behavior near the stable limit cycle solutions. This is because we restrict the type of perturbations that we are considering to allow only for a shift of the LD cycle or a shift of the central oscillator along its own limit cycle. In particular, we don't know if there is an unstable or stable structure outside the basin of attraction of the stable entrained solution without additional analysis. Second, the phase angle method works well with 2-D systems. For higher-dimensional systems, it would require additional assumptions.

Open questions and future directions. This work is based in part on analysis and in part on simulations. We have not proved that the correspondence of the findings of the 2-D map, e.g., existence and stability of fixed points, actually exist for the hierarchical system of

ODEs. We would like to use a 1-D phase model, for example a Kuramoto model [27] for each oscillator, to see if this proof can be made. Alternatively, we believe this method of mapping should be applicable to other models, such as Goodwin [19], Gonze et al. [18], or Forger, Jewett, and Kronauer [17] oscillators which are all higher dimensional. Verifying this, at the moment, would have to rely on checking agreement with simulations. The 2-D entrainment map should also be applicable to understanding the interaction of circadian and sleep-wake rhythms to generalize the findings of Booth, Xique, and Diniz Behn [6].

A necessary condition of our method is the existence of limit cycle solutions of the forced system, so that we can map any point in the phase plane to a point on the limit cycle. Light input is not the only forcing signal that a circadian oscillator receives. For instance, exercise, the intake of meals, and taking melatonin can also be considered as an external forcing. We would like to develop the entrainment map for multiple forcing signals. Another possible direction for future work involves generalization of model reduction techniques. Most reduction techniques are based on weak coupling, such as phase reduction [8]. We would like to develop a technique for a system with strong coupling. This part could potentially be done by deriving a Floquet normal form [10] in phase and amplitude space. For the circadian oscillators that we studied in this paper, it remains open how to derive the Floquet normal form.

REFERENCES

[1] Z. Akcay, A. Bose, and F. Nadim, *Effects of synaptic plasticity on phase and period locking in a network of two oscillatory neurons*, J. Math. Neurosci., 4 (2014), 8.

[2] Z. Akcay, X. Huang, F. Nadim, and A. Bose, *Phase-locking and bistability in neuronal networks with synaptic depression*, Phys. D, 364 (2018), pp. 8–21.

[3] S. An, R. Harang, K. Meeker, D. Granados-Fuentes, C. A. Tsai, C. Mazuski, J. Kim, F. J. Doyle, L. R. Petzold, and E. D. Herzog, *A neuropeptide speeds circadian entrainment by reducing intercellular synchrony*, Proc. Natl. Acad. Sci. USA, 110 (2013), pp. E4355–E4361.

[4] J. Aschoff, *Problems of re-entrainment of circadian rhythms: Asymmetry effect, dissociation and partition*, in Environmental Endocrinology, Springer, Berlin, 1978, pp. 185–195.

[5] R. Ben-Shlomo and B. Kyriacou, *Circadian rhythm entrainment in flies and mammals*, Cell Biochem. Biophys., 37 (2002), pp. 141–156.

[6] V. Booth, I. Xique, and C. G. Diniz Behn, *One-dimensional map for the circadian modulation of sleep in a sleep-wake regulatory network model for human sleep*, SIAM J. Appl. Dyn. Syst., 16 (2017), pp. 1089–1112.

[7] G. Bordyugov, U. Abraham, A. Granada, P. Rose, K. Imkeller, A. Kramer, and H. Herzel, *Tuning the phase of circadian entrainment*, J. R. Soc. Interface, 12 (2015), 20150282.

[8] E. Brown, J. Moehlis, and P. Holmes, *On the phase reduction and response dynamics of neural oscillator populations*, Neural Comput., 16 (2004), pp. 673–715.

[9] O. Castejón and A. Guillamon, *Phase-amplitude dynamics in terms of extended response functions: Invariant curves and Arnold tongues*, Commun. Nonlinear Sci. Numer. Simul., 81 (2020), 105008.

[10] R. Castelli, J.-P. Lessard, and J. D. Mireles James, *Parameterization of invariant manifolds for periodic orbits* I: *Efficient numerics via the floquet normal form*, SIAM J. Appl. Dyn. Syst., 14 (2015), pp. 132–167.

[11] R. Chauhan, K.-F. Chen, B. A. Kent, and D. C. Crowther, *Central and peripheral circadian clocks and their role in alzheimer's disease*, Dis. Models Mechanisms, 10 (2017), pp. 1187–1199.

[12] C. A. Czeisler and E. B. Klerman, *Circadian and sleep-dependent regulation of hormone release in humans.*, Recent Progr. Horm. Res., 54 (1999), pp. 97–130.

[13] C. O. Diekman and A. Bose, *Entrainment maps: A new tool for understanding properties of circadian oscillator models*, J. Biol. Rhythms, 31 (2016), pp. 598–616.
[14] C. O. Diekman and A. Bose, *Reentrainment of the circadian pacemaker during jet lag: East-west asymmetry and the effects of north-south travel*, J. Theoret. Biol., 437 (2018), pp. 261–285.
[15] C. Dubowy and A. Sehgal, *Circadian rhythms and sleep in drosophila melanogaster*, Genetics, 205 (2017), pp. 1373–1397.
[16] J. P. England, B. Krauskopf, and H. M. Osinga, *Computing one-dimensional stable manifolds and stable sets of planar maps without the inverse*, SIAM J. Appl. Dyn. Syst., 3 (2004), pp. 161–190.
[17] D. B. Forger, M. E. Jewett, and R. E. Kronauer, *A simpler model of the human circadian pacemaker*, J. Biol. Rhythms, 14 (1999), pp. 533–538.
[18] D. Gonze, S. Bernard, C. Waltermann, A. Kramer, and H. Herzel, *Spontaneous synchronization of coupled circadian oscillators*, Biophys. J., 89 (2005), pp. 120–129.
[19] B. Goodwin, *Oscillatory behavior in enzymatic control processes*, Adv. Enzyme Regul., 3 (1965), pp. 425–428.
[20] C. Gu, H. Yang, and Z. Ruan, *Entrainment range of the suprachiasmatic nucleus affected by the difference in the neuronal amplitudes between the light-sensitive and light-insensitive regions*, Phys. Rev. E(3), 95 (2017), 042409.
[21] S. Honma, *The mammalian circadian system: A hierarchical multi-oscillator structure for generating circadian rhythm*, J Physiol. Sci., 68 (2018), pp. 207–219.
[22] J. Kim and D. Forger, *A mechanism for robust circadian timekeeping via stoichiometric balance*, Mol. Syst. Biol., 8 (2012), 630.
[23] K. E. Klein, R. Herrmann, P. Kuklinski, and H.-M. Wegmann, *Circadian performance rhythms: Experimental studies in air operations*, in Vigilance, Plenum, New York, 1977, pp. 111–132.
[24] H. Kori, Y. Yamaguchi, and H. Okamura, *Accelerating recovery from jet lag: Prediction from a multi-oscillator model and its experimental confirmation in model animals*, Sci. Rep., 7 (2017), 46702.
[25] K. Kräuchi, *How is the circadian rhythm of core body temperature regulated?*, Clin. Auton. Res., 12 (2002), pp. 147–149.
[26] B. Krauskopf and H. Osinga, *Growing* $1d$ *and quasi-*$2d$ *unstable manifolds of maps*, J. Comput. Phys., 146 (1998), pp. 404–419.
[27] Y. Kuramoto, *Chemical Oscillations, Waves, and Turbulence*, Springer, Heidelberg, 1984.
[28] K. Lee, P. Shiva Kumar, S. McQuade, J. Y. Lee, S. Park, Z. An, and B. Piccoli, *Experimental and mathematical analyses relating circadian period and phase of entrainment in neurospora crassa*, J. Biol. Rhythms, 32 (2017), pp. 550–559.
[29] T. Leise and H. Siegelmann, *Dynamics of a multistage circadian system*, J. Biol. Rhythms, 21 (2006), pp. 314–323.
[30] J.-C. Leloup and A. Goldbeter, *A model for circadian rhythms in drosophila incorporating the formation of a complex between the per and tim proteins*, J. Biol. Rhythms, 13 (1998), pp. 70–87.
[31] H. Levine, *Health and work shifts*, in Shift Work and Health, P. G. Rentos and R. D. Shephard, eds., US Department of Health, Education, and Welfare, Washington, DC, 1976, pp. 57–69.
[32] Y. Lin, G. D. Stormo, and P. H. Taghert, *The neuropeptide pigment-dispersing factor coordinates pacemaker interactions in the drosophila circadian system*, J. Neurosci., 24 (2004), pp. 7951–7957.
[33] C. Mazuski and E. D. Herzog, *Circadian rhythms: To sync or not to sync*, Curr. Biol., 25 (2015), pp. R337–R339.
[34] R. E. Mistlberger and D. J. Skene, *Nonphotic entrainment in humans?*, J. Biol. Rhythms, 20 (2005), pp. 339–352.
[35] H. Nakao, *Phase reduction approach to synchronisation of nonlinear oscillators*, Contemp. Phys., 57 (2016), pp. 188–214.
[36] B. Novák and J. J. Tyson, *Design principles of biochemical oscillators*, Nat. Rev. Mol. Cell Biol., 9 (2008), pp. 981–991.
[37] T. olde Scheper, D. Klinkenberg, C. Pennartz, and J. Van Pelt, *A mathematical model for the intracellular circadian rhythm generator*, J. Neurosci. Res., 19 (1999), pp. 40–47.
[38] S. Risau-Gusman and P. M. Gleiser, *A mathematical model of communication between groups of circadian neurons in drosophila melanogaster*, J. Biol. Rhythms, 29 (2014), pp. 401–410.

[39] L. Roberts, T. L. Leise, D. K. Welsh, and T. C. Holmes, *Functional contributions of strong and weak cellular oscillators to synchrony and light-shifted phase dynamics*, J. Biol. Rhythms, 31 (2016), pp. 337–351.

[40] K. Tsumoto, T. Yoshinaga, H. Iida, H. Kawakami, and K. Aihara, *Bifurcations in a mathematical model for circadian oscillations of clock genes*, J. Theoret. Biol., 239 (2006), pp. 101–122.

[41] J. J. Tyson, C. I. Hong, C. D. Thron, and B. Novak, *A simple model of circadian rhythms based on dimerization and proteolysis of per and tim*, Biophys. J., 77 (1999), pp. 2411–2417.